Earthquake source scaling and self-similarity estimation from stacking *P* and *S* spectra

Germán A. Prieto, Peter M. Shearer, Frank L. Vernon, and Debi Kilb

Institute of Geophysics and Planetary Physics, Scripps Institution of Oceanography, University of California, San Diego, La Jolla, California, USA

Received 12 March 2004; revised 18 June 2004; accepted 29 June 2004; published 28 August 2004.

[1] We study the scaling relationships of source parameters and the self-similarity of earthquake spectra by analyzing a cluster of over 400 small earthquakes (M_L = 0.5 to 3.4) recorded by the Anza seismic network in southern California. We compute *P*, *S*, and preevent noise spectra from each seismogram using a multitaper technique and approximate source and receiver terms by iteratively stacking the spectra. To estimate scaling relationships, we average the spectra in size bins based on their relative moment. We correct for attenuation by using the smallest moment bin as an empirical Green's function (EGF) for the stacked spectra in the larger moment bins. The shapes of the log spectra agree within their estimated uncertainties after shifting along the ω^{-3} line expected for self-similarity of the source spectra. We also estimate corner frequencies and radiated energy from the relative source spectra using a simple source model. The ratio between radiated seismic energy and seismic moment (proportional to apparent stress) is nearly constant with increasing moment over the magnitude range of our EGF-corrected data (M_L = 1.8 to 3.4). Corner frequencies vary inversely as the cube root of moment, as expected from the observed self-similarity in the spectra. The ratio between *P* and *S* corner frequencies is observed to be 1.6 ± 0.2. We obtain values for absolute moment and energy by calibrating our results to local magnitudes for these earthquakes. This yields a *S* to *P* energy ratio of 9 ± 1.5 and a value of apparent stress of about 1 MPa.

INDEX TERMS: 7215 Seismology: Earthquake parameters; 7209 Seismology: Earthquake dynamics and mechanics; 7299 Seismology: General or miscellaneous; *KEYWORDS:* spectrum, source parameters, self-similarity

Citation: Prieto, G. A., P. M. Shearer, F. L. Vernon, and D. Kilb (2004), Earthquake source scaling and self-similarity estimation from stacking *P* and *S* spectra, *J. Geophys. Res.*, *109*, B08310, doi:10.1029/2004JB003084.

1. Introduction

[2] A major question in seismology is whether the faulting mechanism of large and small earthquakes involves different physics. That is, is a $M = 8$ earthquake just a $M = 2$ earthquake scaled upward by a large factor or is something fundamentally different occurring? *Aki* [1967] proposed scale invariance of the rupture process, consistent with observations that many geological processes are similar over a wide range of scales [*Abercrombie*, 1995]. There is currently a debate regarding whether earthquakes are truly self-similar over their entire size range or if systematic departures from self-similarity are observed [see, e.g., *Abercrombie*, 1995; *Ide and Beroza*, 2001]. Thus, although many mechanisms have been proposed for differences in the physics of larger earthquakes, including shear melting [*Jeffreys*, 1942; *Kanamori and Heaton*, 2000], acoustic fluidization [*Melosh*, 1979], rough fault sliding-induced normal stress reduction [*Brune et al.*, 1993], fluid pressurization [*Sibson*, 1973], and elastohydrodynamic lubrication [*Brodsky and Kanamori*, 2001], the need for different mechanisms is not yet firmly established.

[3] Studies of earthquake scaling generally involve comparisons between static measures of size (e.g., moment) and dynamic measures of size (e.g., energy). Both measures are typically derived from spectra of seismograms recorded at some distance from the earthquakes. Because moment is obtained from the low frequency part of the spectra, it is usually measured much more reliably than energy or corner frequency measurements, which require the high-frequency part of the spectra where correcting for attenuation and other path effects can be difficult. Current estimates of seismic moment made independently from local, regional and teleseismic data usually agree within about a factor of 2. In contrast, estimates of seismically radiated energy by different investigators for the same earthquake often differ by more than an order of magnitude [e.g., *Singh and Ordaz*, 1994; *Mayeda and Walter*, 1996].

[4] This uncertainty in seismic energy leads to different interpretations of the energy density of earthquakes, as measured by the energy/moment ratio, which is often scaled by rigidity to represent the apparent stress. Several authors find evidence that apparent stress increases with magnitude [*Kanamori et al.*, 1993; *Abercrombie*, 1995; *Mayeda and*

Copyright 2004 by the American Geophysical Union.
0148-0227/04/2004JB003084$09.00

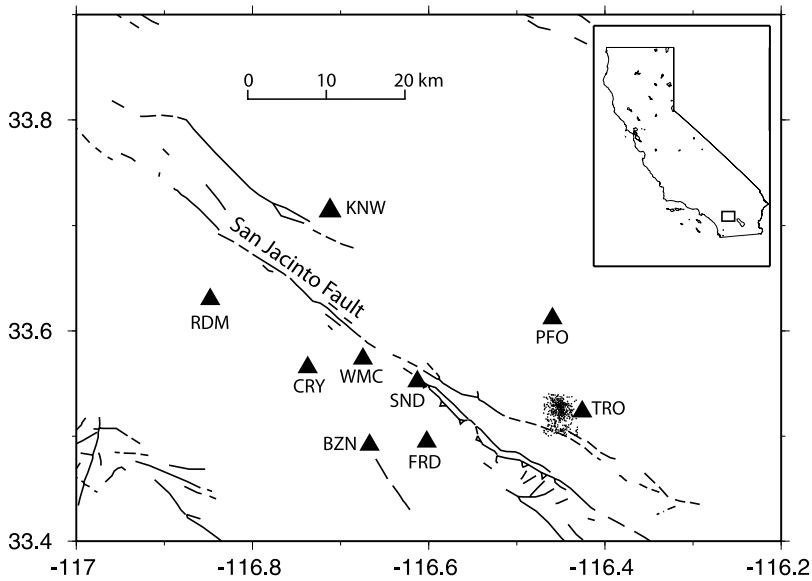

Figure 1. Map showing the cluster of over 400 earthquakes (small black dots) and Anza stations (solid triangles) used in this study. The inset shows the location of the study area (rectangle) in the state of California.

Walter, 1996; *Izutani and Kanamori*, 2001; *Mori et al.*, 2003], while others argue that apparent stress is approximately constant [*Choy and Boatwright*, 1995; *McGarr*, 1999; *Ide and Beroza*, 2001; *Ide et al.*, 2003]. Constant apparent stress implies similar physics for small and large earthquakes, while increasing apparent stress with magnitude implies that earthquakes are more efficient radiators of seismic energy than small ones.

[5] Our approach here is to improve the reliability and stability of source spectra by stacking and averaging thousands of records from the Anza seismic network in southern California. We use a simple method [*Warren and Shearer*, 2000, 2002] to isolate the relative source spectra from the path and site effects by stacking the computed log spectra after subtracting the appropriate path-site terms. This approach is also similar to that used by *Andrews* [1986] to analyze spectra of the 1980 Mammoth Lakes California earthquake sequence. Rather than obtaining an absolute measure of individual source spectra, we obtain relative shapes of spectra with respect to other earthquakes. We then stack the spectra in bins of similar moment to obtain average spectra (and estimated uncertainties) as a function of earthquake size and apply attenuation corrections using the smallest earthquakes as empirical Green's functions (EGF) [e.g., *Mueller*, 1985; *Hough*, 1997]. The resulting spectra are sufficiently smooth that direct tests of the self-similarity hypothesis are possible, as well as measurements of corner frequency and energy. All of our results indicate self-similarity is closely obeyed over the M_L = 1.8 to 3.4 size range of our EGF-corrected data.

2. Data Processing

[6] We used records from the Anza seismic network [*Berger et al.*, 1984; *Vernon*, 1989], 9 high-quality, three-component stations located on hard rock sites near an active part of the Clark Lake segment of the San Jacinto fault in southern California (Figure 1). We began this study by selecting about 800 earthquakes located in a tightly clustered volume (4.5 km sided area, with most of the events between 5 and 12 km depth) near the Toro Peak station (TRO) and 50 km from the most distant station (RDM). In this region, the database is complete to about $M_L \geq 0.5$ with generally good signal-to-noise ratio records. The earthquakes occurred from 1983 to 1993, at which time the network recorded at 250 samples per second with Geospace HS−10, 2-Hz seismometers. We selected a relatively compact group of earthquakes so that the path to each station would be similar between different earthquakes, permitting the use of simple corrections for attenuation and other path effects.

[7] We use both *P* and *S* waves and select time windows for *P* on the vertical component and time windows for *S* on all three components. Both windows start 0.5 s before the analyst pick of the arrival, with a total window length of 1.28 s. We also select a noise window of the same length, with the last data point just before the *P* wave window. The velocity spectrum is estimated using the multitaper algorithm [*Park et al.*, 1987] and then corrected for the instrument response function. The *S* wave spectrum is calculated as the vector summation of spectra from all three components. Figure 2 shows an example of this process for a vertical component record from station FRD.

[8] We apply a signal-to-noise ratio cutoff, where we use spectra only when the mean ratio is greater than 5.0 in the 0−80 Hz frequency band and the ratio is greater than 3.0 at 80 Hz. At higher frequencies, the signal-to-noise ratio decreases very rapidly (see Figure 2), so we limit our analysis to frequencies below 80 Hz. After applying the cutoff, we have 2735 records (including both *P* and *S* waves) from 470 earthquakes. Because of their larger amplitudes, the *S* waves have generally higher signal-to-noise ratios than the *P* waves; thus our signal-to-noise cutoff

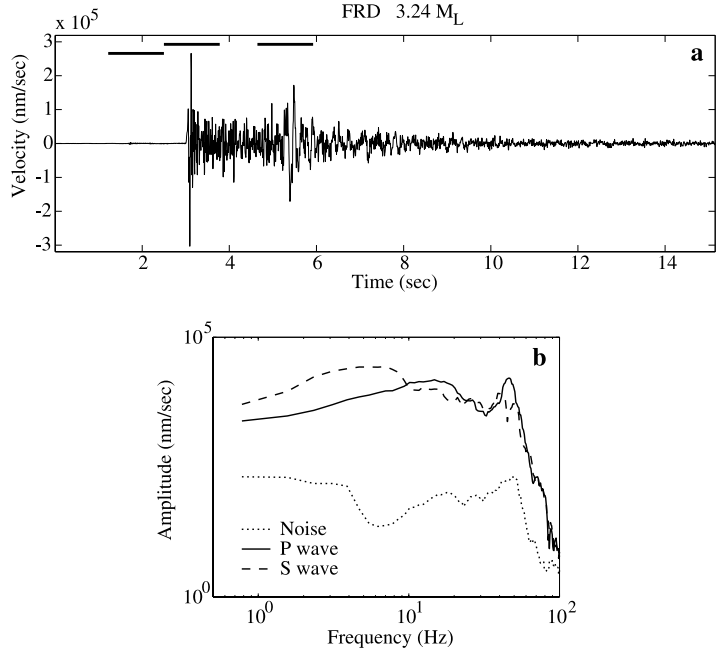

Figure 2. Example of computed spectra from the largest magnitude earthquake in the study area (M_L = 3.4) recorded at station FRD, vertical component. (a) The time series, with horizontal bars showing the noise, *P*, and *S* windows used to compute the spectra. In this case the *S* wave shows up more clearly on the horizontal components. (b) Spectra for the windows shown in Figure 2a, computed using a multitaper method. Note the rapid decrease in signal-to-noise ratio at the higher frequencies.

excludes *P* waves from the smallest earthquakes in our data set, which are represented only by *S* wave spectra.

[9] One possible concern is that *P* wave coda may be contaminating the *S* wave window. This potential source of bias is likely to have its largest effect on the closest stations where the $S - P$ time is the smallest. To test what effect this may be having on our results, we repeated our analyses using subsets of the data where we removed the closest, the two closest and the four closest stations from the source region. Although there was some increase in the variability of the stacked spectra as we reduced the number of data in the stacks, there were no systematic changes in the *S* spectral shapes. Thus it does not appear that *P* contamination of *S* is a significant factor in our analyses.

[10] Since multiple stations record every earthquake and many earthquakes are recorded at each station, we can isolate the source and receiver contributions to the spectra. Because our source region is relatively compact, the receiver contributions will also include most of the path effects. Following the method described by *Warren and Shearer* [2002], it is possible to isolate the relative source spectrum (Figure 3) if we assume that the observed spectrum $D_{ij}(f)$ from each source and receiver (denoted S_i for the *i*th earthquake and R_j for the *j*th station) is a product of source effects and path-site effects. We iteratively stack all log spectra from each earthquake, after removing the appropriate station term, to obtain the earthquake term:

$$\log(S_i) = \frac{1}{n}\sum_{j=1}^{n}\left[\log(D_{ij}) - \log(R_j)\right] \quad (1)$$

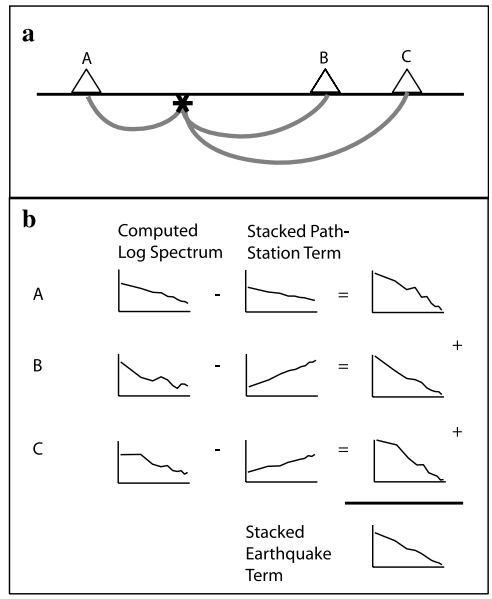

Figure 3. Cartoon explaining how spectral stacking is used to obtain the earthquake term, as by *Warren and Shearer* [2002]. If a given earthquake (star) is recorded at stations A, B, and C (Figure 3a), the earthquake term is computed by stacking the log spectrum from earthquake 1 computed for stations A, B, and C after removing the path-station terms for these stations (Figure 3b). An analogous procedure is used to compute the station terms.

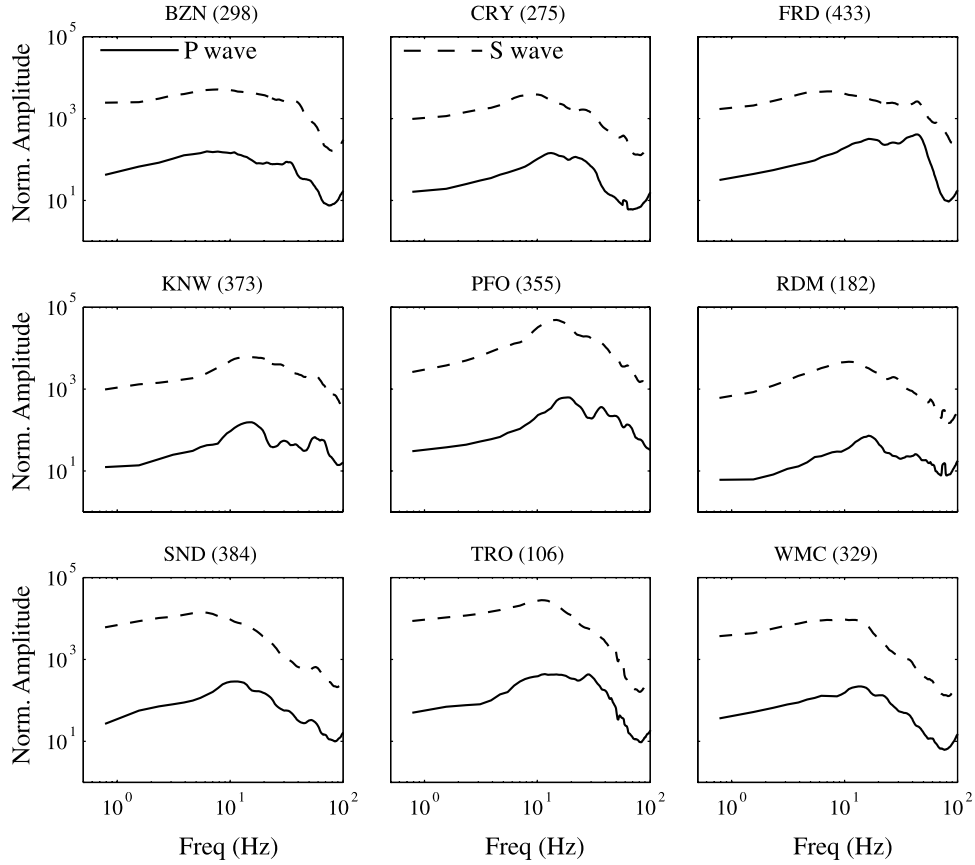

Figure 4. Examples of path-station terms for *P* (solid line) and *S* (dashed line) waves. The number of earthquakes recorded at each particular station is given in parentheses. Note that the path-station term for the *S* waves is always larger, reflecting the higher amplitude of *S* compared to *P*.

and we also stack all log spectra from each station, after removing the earthquake term, to obtain the path-station term:

$$\log(R_j) = \frac{1}{m}\sum_{i=1}^{m}\left[\log(D_{ij}) - \log(S_i)\right] \quad (2)$$

where D_{ij} is the computed spectrum, S_i the earthquake term for the ith earthquake, and R_j the path-station term for the jth station. Since the earthquake term and the path-station term are dependent upon each other, we solve the set of equations iteratively until we reach a stable result, where the fractional change in either the source or path-station terms is less than 10^{-4}. We normalize the average log source spectra for all our earthquakes to unity, as a starting point for the iteration process. In practice, we are mapping the deviations of the source spectra from this reference flat spectrum.

[11] After source and path-station terms are separated we obtain 470 relative source spectra and 9 path-station spectra (separately for *P* and *S* waves). Figure 4 shows the *P* and *S* path-site spectra for nine different stations. Because we have not yet assumed a source model (e.g., ω^{-2}, etc.), the shape of each of these spectra will include both source and attenuation contributions. The information is contained in the differences between these curves, which are significant because all of the stations recorded the same set of earthquakes. Variations in attenuation among the stations can be seen in the position at which the spectra begin to falloff at high frequencies. For example, it is clear that station SND, located within 100 meters of the surface trace of the San Jacinto fault, records a more attenuating path than station FRD, despite the fact that FRD is located slightly closer to the earthquake cluster. In general, there is no clear distance dependence to the observed path-station spectra, suggesting that local site effects beneath each station are dominating the spectral differences among the stations.

[12] Each of the 470 relative source spectra represents the average log spectra of all stations recording the earthquake, after correcting for differences among the path-station terms. To study how these source spectra vary as a function of earthquake size, we divide our data into 20 bins in relative moment, which is estimated from the low-frequency spectral amplitude. Because our *S* wave data span a larger total moment range than the *P* wave data, the moment range within each *S* wave bin is larger than in the *P* wave bins. At this stage in our analysis, we do not compare *P* and *S* amplitudes directly; rather we process the *P* and *S* spectra separately and obtain independent results for each phase (later comparisons between *P* and *S* corner frequencies will jointly consider the data).

[13] Selected *S* wave results are plotted in Figure 5a. Each binned source spectra is the result of averaging between 1 and 86 earthquake spectra (each of which is itself a stack of spectra from different stations recording the earthquake). The resulting binned source spectra are much smoother than

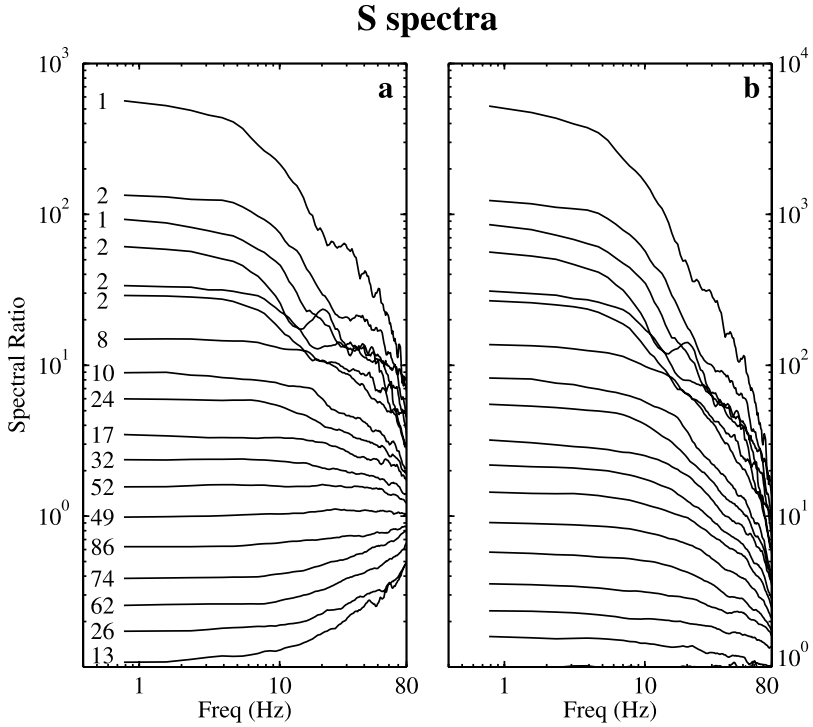

Figure 5. Relative source spectral shapes for some selected bins. (a) Shapes relative to the average spectra, which were forced to have a constant log amplitude of 1. Numbers to the left of each spectra indicate the number of earthquakes in that particular bin. (b) Corrected source shapes, after applying the smallest magnitude bin as an empirical Green's function (EGF). To avoid passing unwanted line components present in the smallest bin, we smoothed the reference spectrum with a 20-point moving average before subtracting it from the data.

the individual spectra that go into the stacks. There are generally many more earthquakes in the bins at smaller moments because of the much larger number of smaller earthquakes in the data set. The relative moments among the bins can be seen in the low-frequency limit of the spectra (i.e., at about 1 Hz). These moments are not evenly spaced in Figure 5 because the moments of the earthquakes within each bin are not always evenly distributed. We use a bootstrap technique that randomly resamples the earthquakes within each source spectral bin in order to estimate uncertainties on the binned spectra, and later to estimate uncertainties on properties, such as corner frequency and energy, that we compute from these spectra.

[14] As in the case of the path-site terms, the absolute shape of the spectra plotted in Figure 5a is unconstrained (owing to the intrinsic tradeoff between the average source spectrum and the average path-site response function). We resolve this tradeoff in our iterative method by forcing the average source spectrum to unity. This is why the spectra for the small earthquake bins curve upward at high frequency. This indicates that, as expected, these earthquakes have a shallower falloff at high frequencies compared to larger earthquakes. To obtain an estimate of the true spectral shapes of the sources, we use the smallest moment bin as an empirical Green's function (EGF) for all the other bins.

[15] Figure 5b shows the results of subtracting the log spectra of the smallest bin from the others. These EGF-corrected spectra have the features expected for source spectra: a flat response out to a corner frequency that increases with decreasing earthquake size and a rapid falloff beyond the corner frequency. As we will discuss later this falloff closely agrees with the Brune ω^{-2} source model [*Brune*, 1970]. We plot all of the EGF-corrected spectra in Figure 5, but our later analyses will focus only on those bins at least one order of magnitude larger in moment than the EGF reference bin. For comparison, *Mori et al.* [2003] used a $M \sim 1.5$ smaller EGF and *Frankel et al.* [1986] used earthquakes with $M \leq 2.1$ as EGF of $M \sim 3$ earthquakes. As previously noted, because of signal-to-noise limitations, we do not use *P* wave data from the smallest earthquakes so the smallest *P* wave EGF bin represents the same bin as the third smallest *S* wave EGF bin.

3. Implications of Self-Similarity

[16] Before further analysis, it is instructive to consider the predicted effects of earthquake self-similarity on recorded spectra [e.g., *Aki*, 1967]. Figure 6 illustrates the expected change in the pulse shape and spectrum for an earthquake rupture that is increased in size by a factor b. Assuming the dimensions of the larger rupture are scaled proportionally, then the fault area, A, will increase by a factor b^2, the displacement, D, will increase by b, and the moment, $M_0 = \mu DA$, will increase by a factor of b^3. Figure 6b shows the resulting change in a displacement pulse, $u(t)$, recorded in the far field, assuming identical source and receiver locations and no attenuation. The exact form of the shape of this pulse depends upon details of the source, but assuming simple

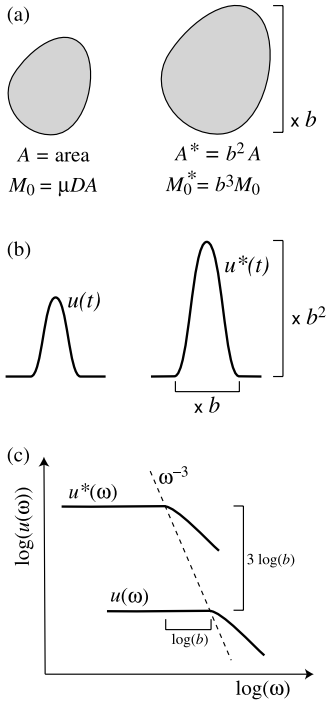

Figure 6. Illustration of the effects of self-similarity when an earthquake is increased in size by a factor of b. (a) Rupture area, which increases by b^2, the displacement, which increases by b, and the moment and energy, which increase by b^3. (b) A recorded far-field displacement pulse, which will increase in length by b and in height by b^2. (c) Log-log plots of the spectra, which will have identical shapes but shifted along an ω^{-3} line.

scaling between the two earthquakes, the pulse shape will change in a predictable way. In particular, assuming the rupture speed is constant between the earthquakes (as simple self-similarity predicts), the pulse length will increase by a factor of b and the pulse height will increase by a factor of b^2. This is necessary in order for the moment, which is proportional to the integrated area under the pulse, to increase by b^3.

[17] It follows that the displacement pulse, u^*, recorded by the second earthquake can be expressed as

$$u^*(t) = b^2 u(t/b) \tag{3}$$

where $u(t)$ is the recorded displacement pulse of the first earthquake. The seismic energy, E_s, in the recorded pulse will be proportional to $\int \dot{u}^2(t)\, dt$ (the integrated square of the slope of the pulse), so the second pulse will contain a factor b^3 more energy than the first pulse. Thus the energy density (E_s/M_0) remains constant.

[18] Using the similarity theorem for the Fourier transform, it follows that the spectrum of the second earthquake is given by

$$u^*(\omega) = b^3 u(b\omega) \tag{4}$$

where $u(\omega)$ is the spectrum of the first earthquake. This relationship predicts that the shape of all spectra on a log-log plot will be identical but offset along a line of ω^{-3} (Figure 6c).

[19] This provides a possible test of self-similarity that does not depend upon any assumptions regarding which source model is most appropriate (ω^{-2}, ω^{-3}, etc.). We perform this test (Figure 7) by shifting the EGF-corrected spectra along an ω^{-3} line and find that the shapes are in agreement within their estimated uncertainties. Furthermore, there is no systematic dependence with moment exhibited in the alignment of the binned spectra (Figures 7c and 7d). The P wave spectra do not align as closely as the S wave spectra at low frequencies ($\leq$1 Hz) because the individual P wave stacks are not flat at low frequencies (Figure 7a). Although we do not fully understand the reason for this behavior, the shapes of the P spectra are nonetheless similar within their uncertainties. It is likely that this anomaly in the P wave spectra is related to decreasing signal-to-noise ratios at low frequencies, which could bias the EGF reference stack because it is derived from the smallest earthquakes.

[20] The S wave spectra are noticeably smoother and provide our most reliable constraints on the similarity of the spectra as a function of moment. This is the most fundamental result in our study and suggests the self-similarity hypothesis is valid for our data set. The great advantage of this analysis is that we can check if spectral shapes are self-similar or if there are systematic differences in the shapes as magnitude increases, without assuming a particular model of corner frequency and high-frequency falloff. In contrast, conventional methods for making inferences about source scaling are heavily focused on parametric data derived from the spectra rather than the spectra themselves. These parameters do, however, provide further insight regarding source properties.

[21] Implicit in our spectral comparisons is that the focal mechanisms and rupture directions do not vary systematically between smaller and larger earthquakes because this could bias the results obtained at particular stations. We have not examined the focal mechanisms for our earthquakes, but we have no evidence that this is the case. Such problems are likely to be minimized in our analysis because we are averaging results from many stations at different azimuths and distances from the earthquakes. Furthermore, it seems unlikely that these possible biases would have the effect of producing apparent self-similarity in our measured spectra without self-similarity being present in the earthquakes themselves.

4. Source Parameter Modeling

[22] The source parameters seismic moment (M_0), corner frequency (f_c), and radiated energy (E_s) can be estimated from the source spectra and are important in the understanding of the physics of the earthquake source, as well as for computing apparent stress (σ_a), defined as $\mu E_s/M_0$, where μ is the rigidity. If self-similarity holds, as tested in section 3, this ratio should remain constant over the same range of magnitudes.

[23] We initially fit our P and S displacement spectral stacks with a general source model [e.g., *Abercrombie*, 1995]:

$$u(f) = \frac{\Omega_0}{\left[1 + \left(\frac{f}{f_c}\right)^{\gamma n}\right]^{1/\gamma}} \tag{5}$$

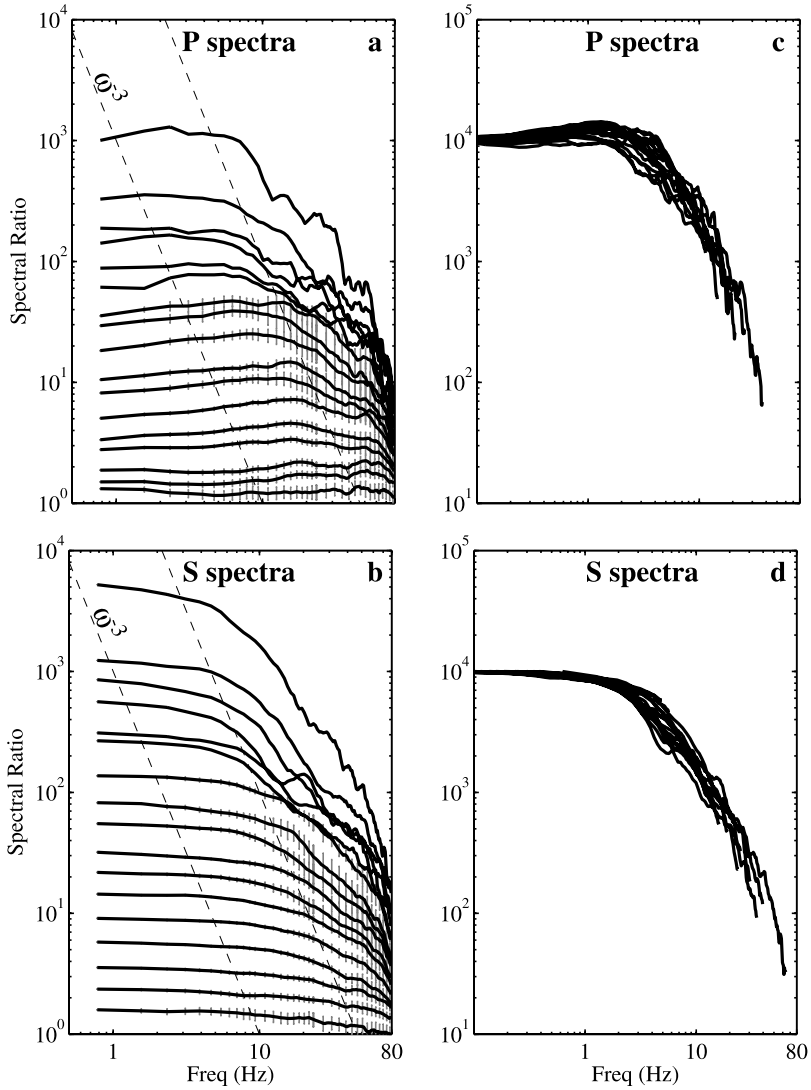

Figure 7. EGF-corrected stacked spectra for bins of different source moment, showing the self-similarity of the spectra when shifted along an ω^{-3} line. (a) *P* wave spectra and (b) *S* wave spectra, with 1-σ error bars estimated using a bootstrap resampling method. The spectra shifted along an ω^{-3} line (dashed lines at left) for (c) *P* waves and (d) *S* waves. The spectra agree in shape within their estimated errors, consistent with the earthquake self-similarity hypothesis.

where Ω_0 is the long-period amplitude (relative seismic moment), f is the frequency, f_c is the corner frequency, n is the high-frequency falloff rate, and γ is a constant. We allowed the values of n to vary while using $\gamma = 1$ as well as $\gamma = 2$; that is, we experimented with both the *Brune* [1970] and *Boatwright* [1980] models, allowing the falloff term to vary as well as corner frequency and relative seismic moment. We used a grid search technique to find the best fitting set of parameters (Ω_0, f_c, n, and γ). We restricted this procedure to those size bins that have relative moments 10 times larger than that of the EGF bin (see Figure 5).

[24] In general, we found that a simple ω^{-n} model (i.e., $\gamma = 1$) worked reasonably well with values of n ranging from 1.8 to 2.2 (i.e., very close to the Brune ω^{-2} model) and that allowing additional free parameters did not significantly improve the fit. Predictions obtained using $\gamma = 2$ yielded spectra with sharper corners than are seen in our stacked spectra. It is possible that individual events have spectra with these sharp corners, but given some variability in the positions of the corners, the corner is smoothed and widened in the stacks over many events so that the Brune model gives the best fit. We therefore used the model

$$u(f) = \frac{\Omega_0}{1 + (f/f_c)^n} \tag{6}$$

and solved for the best fitting Ω_0, f_c, and n for the results presented here (see Figure 8 for examples of the resulting fits to the stacked spectra).

[25] The radiated seismic energy is proportional to $\int \dot{u}^2(t)\, dt$, the integrated square of the measured velocity. We perform this calculation in the frequency domain by converting the displacement spectra to velocity, squaring and integrating [e.g., following *Ide and Beroza*, 2001], being

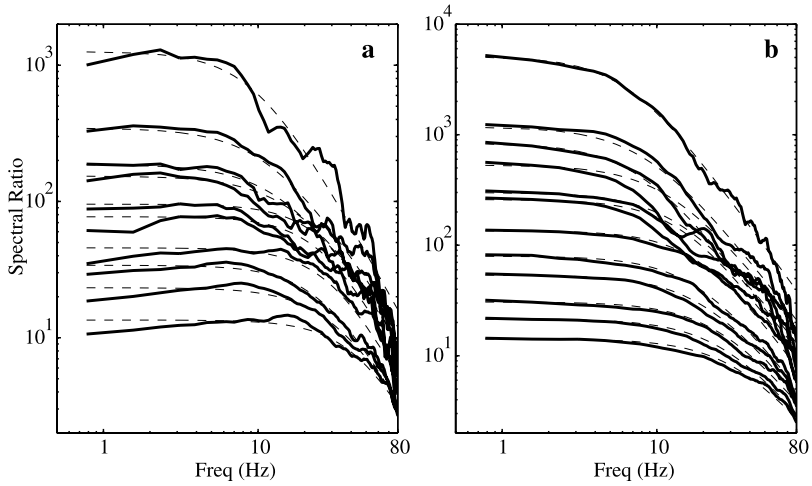

Figure 8. EGF-corrected stacked spectra and best fitting source models for (a) *P* waves and (b) *S* waves. For clarity, only some of the moment bins are plotted.

careful to extrapolate to very high frequencies using the model falloff rate. In this study we compute energy from the best fitting model rather than directly from the data; that is, we use

$$I = \int_0^\infty \left[\frac{2\pi f \Omega_0}{1 + (f/f_c)^n}\right]^2 df \tag{7}$$

where I is the relative seismic energy. Because we are integrating the model-predicted spectrum rather than the data, we can extend the upper integration limit to a sufficiently high frequency to avoid any underestimation of the energy.

5. Calibration to Absolute Moment and Energy

[26] Our results described so far involve only relative estimates of moment and seismic energy. To obtain absolute measures of these parameters directly from our data, we would need to apply corrections for geometrical spreading, radiation pattern, free surface, and source-receiver impedance contrast effects. Because these corrections are often difficult to estimate precisely, this will introduce considerable uncertainty into our results. However, because our earthquakes are in a single compact region, these correction factors are likely to be highly correlated, implying that relative measures of moment and energy among our earthquakes are determined more accurately than their absolute level. Thus our most precise results involve relative measurements among our earthquakes. However, for comparisons to other studies it is useful to have some measure of absolute moment and energy. Our approach to this problem is to exploit the fact that these earthquakes were also recorded by the Southern California Seismic Network (SCSN), which provides well-calibrated local magnitude estimates (moment is not routinely computed for earthquakes this small).

[27] Assuming that $M_L \approx M_W$, we can estimate moment M_0 using the *Kanamori* [1977] relation

$$M_W = (2/3)\log_{10} M_0 - 10.7 \tag{8}$$

In this way, we can compute a scaling factor to relate our relative moment estimates Ω_0 to local magnitude and to true moment M_0. A comparison between SCSN mean catalog M_L versus our estimated M_L (Figure 9) shows a linear relationship with a slope close to unity, as expected if the 2/3 factor in equation (8) is accurate. Previous studies have shown that in the magnitude range of our data set, a linear relation between $\log(M_0)$ and M_W fits the data in southern California, although with some variations on the 2/3 factor (see *Hanks and Boore* [1984] and *Abercrombie* [1996] for more detailed discussion). A change in the scaling factor would change the absolute moment magnitude after calibration, but the relative moment between the different earthquake bins should remain constant.

[28] Now consider the theoretical relationships for M_0 and E_s for a double-couple source in the far field in a uniform whole space. The standard formula [e.g., *Aki and Richards*, 1980; *Kanamori and Rivera*, 2004] for the moment in this case is

$$M_0 = 4\pi\rho c^3 r_c U_{\phi\theta}^{-1}\, \Omega_0 \tag{9}$$

where ρ is the density, c is the seismic velocity (either α for *P* wave or β for *S* wave), r is the source-receiver distance, ${}_cU_{\phi\theta}$ is the radiation pattern, and Ω_0 is the observed long-period amplitude. Now assume that we know M_0, ρ, and c independently. We can then rewrite equation (9) as

$$\frac{{}_cU_{\phi\theta}}{r} = 4\pi\rho c^3 \frac{\Omega_0}{M_0} \tag{10}$$

Note that $1/r$ represents a geometrical spreading term that could be generalized to a more complicated model.

[29] For the same whole-space double-couple model, the radiated seismic energy may be expressed as [e.g., *Boatwright and Fletcher*, 1984]

$$E_s^c = 4\pi\rho c r^2 \frac{\langle {}_cU_{\phi\theta}^2 \rangle}{{}_cU_{\phi\theta}^2} I \tag{11}$$

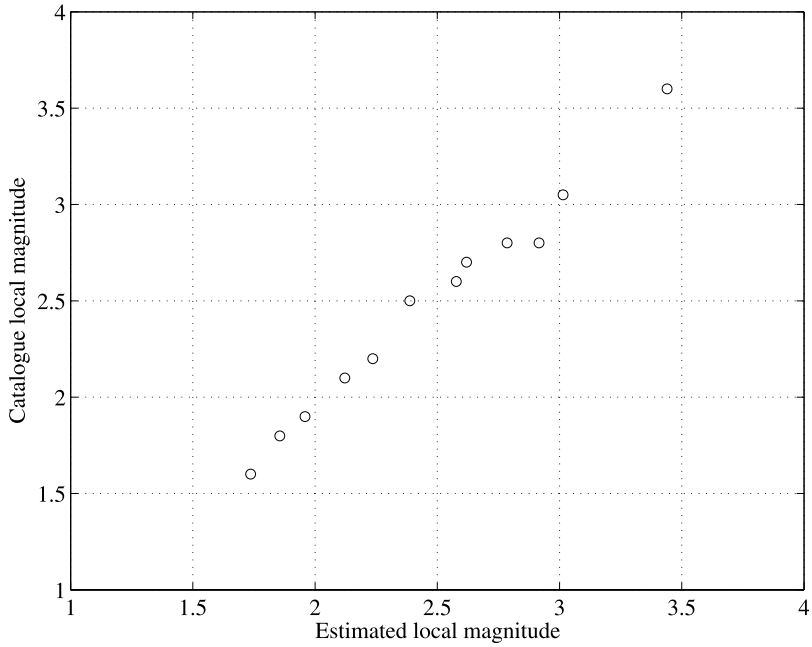

Figure 9. Comparison between M_L as measured by the Southern California Seismic Network (SCSN) and M_L as estimated from our relative moment measures using an empirical scaling factor.

where $\langle {}_cU^2_{\phi\theta}\rangle$ is the mean over the focal sphere of $({}_cU_{\phi\theta})^2$ (=4/15 for P waves and 2/5 for S waves) and I is the measured relative energy (i.e., the integrated velocity squared). Because this equation involves the ratio of ${}_cU_{\phi\theta}$ and r, we can use equation (10) to obtain

$$E_s^c = \frac{\langle {}_cU^2_{\phi\theta}\rangle}{4\pi\rho c^5} M_0^2 \frac{I}{\Omega_0^2} \tag{12}$$

which is independent of the geometrical spreading and radiation pattern terms. This equation remains accurate if free surface corrections are applied or if the instrument gain is incorrectly known, provided M_0 is determined independently. In the case where ρ and c vary between source and receiver, carrying through the impedance correction terms shows that equation (12) is still valid provided ρ and c are taken at the source.

[30] Because the estimated energy varies inversely as c^5, the results are very sensitive to errors in velocity at the source. A 15% error in c will produce about a factor of 2 error in E_s. In this study we use $\alpha = 6.0$ km/s, $\beta = \alpha/\sqrt{3}$, and $\rho = 2.7$ kg/m^3, which leads to the value $\mu = 3.24 \times 10^{10}$ Pa. The values of velocity are very close to those from a three-dimensional seismic velocity inversion [*Scott et al.*, 1994] for the source region. We estimate the uncertainty in our source velocity estimates to be less than 5%.

[31] The total radiated seismic energy is obtained by adding the energy for P and S waves

$$E_s = E_s^P + E_s^S \tag{13}$$

Finally, it is important to recognize that absolute energy estimates are also very sensitive to attenuation corrections. We assume here that the EGF approach has correctly removed attenuation effects, but this remains another possible source of uncertainty in our results.

6. Results for Corner Frequency and Apparent Stress

[32] To compare P and S corner frequencies, we performed a separate analysis in which the relative moment of each earthquake was estimated from both the P and S spectra so that the same earthquakes would be contained in each moment bin. As discussed in section 5, this relative moment will later be calibrated with estimates of moment from local magnitude determinations. We find that the P wave corner frequencies determined here are systematically higher than those estimated for S waves from the same earthquakes (Figure 10). The ratio $f_c(P)/f_c(S)$ is about 1.6 (individual measurements range from 1.3 to 2.0), consistent with the model of *Madariaga* [1976] and very close to values determined using borehole recordings at 2.5-km depth in the Cajon Pass, California, by *Abercrombie* [1995]. This ratio is likely to correspond principally to source effects since attenuation and other path-site effects have been removed.

[33] As analyzed by *Abercrombie* [1995], the ratio of S to P wave energy (known as q) is also very important. From *Boatwright and Fletcher* [1984] we have

$$q = \frac{3}{2}\left(\frac{\alpha}{\beta}\right)^5 \left(\frac{f_c(S)}{f_c(P)}\right)^3 \tag{14}$$

where $f_c(S)$ and $f_c(P)$ are the corner frequencies for S and P (which are assumed to have the same falloff rate at high frequencies). Note that $q = 23.4$ for a Poisson solid if the corner frequencies are identical. In our study, $f_c(P)$ is about

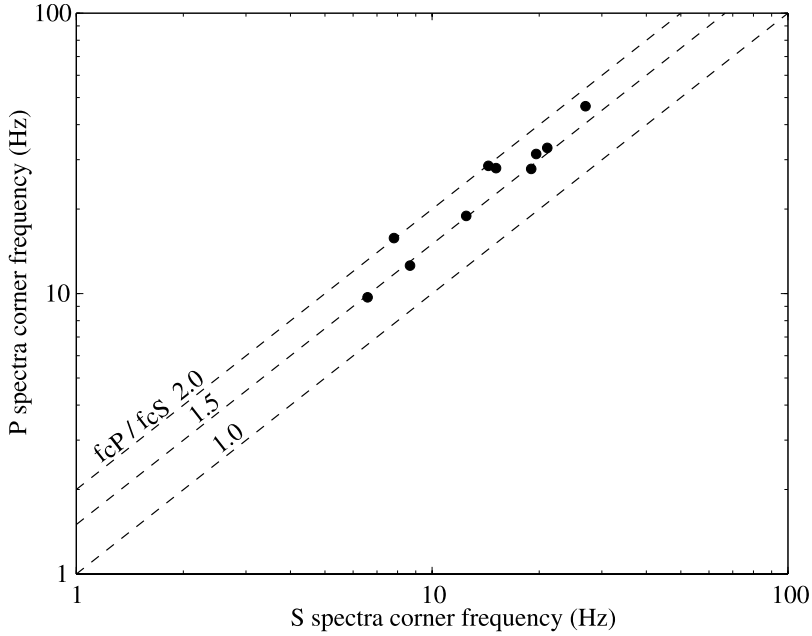

Figure 10. Comparison between *P* and *S* wave corner frequencies as measured for the different moment bins. Dashed lines represent different scaling factors. The data suggest $f_c(P) \approx 1.6 f_c(S)$.

1.6 times larger than $f_c(S)$, reducing the predicted value of q to about 6.

[34] Our estimated *P* and *S* energies (Figure 11), calculated using equation (12) for the different moment bins, yield $q = 9 \pm 1.5$, the difference from the predicted value ($q = 6$) resulting from the fact that our models permit the falloff exponent to vary slightly between *P* and *S* waves. Previous studies have found considerable variation in q estimates, as they are highly dependent upon corner frequency shifts, but our results are in reasonable agreement with, for example, *Boatwright and Fletcher* [1984] ($q = 13.7 \pm 7.3$) and *Abercrombie* [1995] ($q = 14.31$ with values from 4.43 to 46.26). We did not directly obtain *P* wave energy for the two smallest spectral bins because their relative moment was not 10 times larger than the *P* wave EGF. To obtain *P* energy for these bins, we divided the *S* wave energy by the $q = 9$ scaling parameter estimated from the other bins.

[35] Another commonly applied test of self-similarity [e.g., *Abercrombie*, 1995; *Ide et al.*, 2003; *Kanamori and*

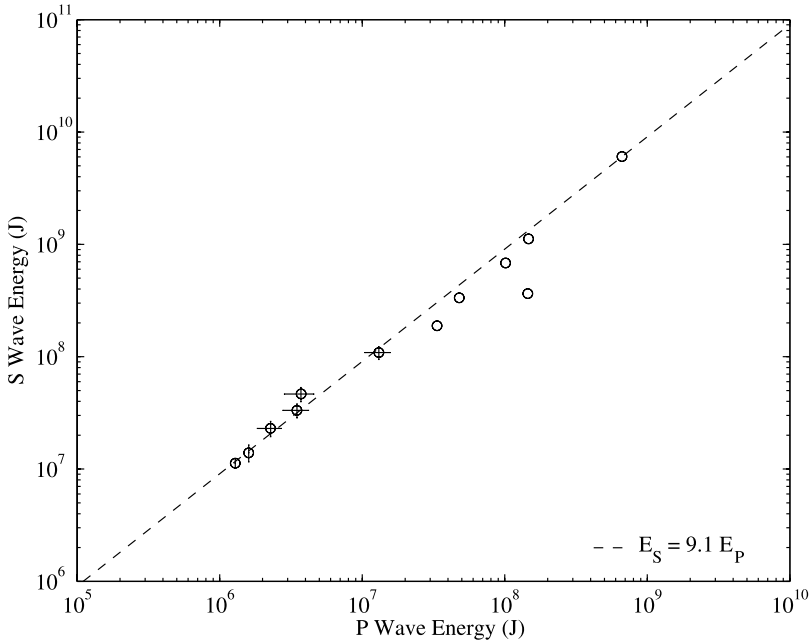

Figure 11. Radiated *S* wave energy E_s^S versus *P* wave energy E_s^P estimated from the different moment bins. The best fitting line is for $E_s^S = 9\ E_s^P$.

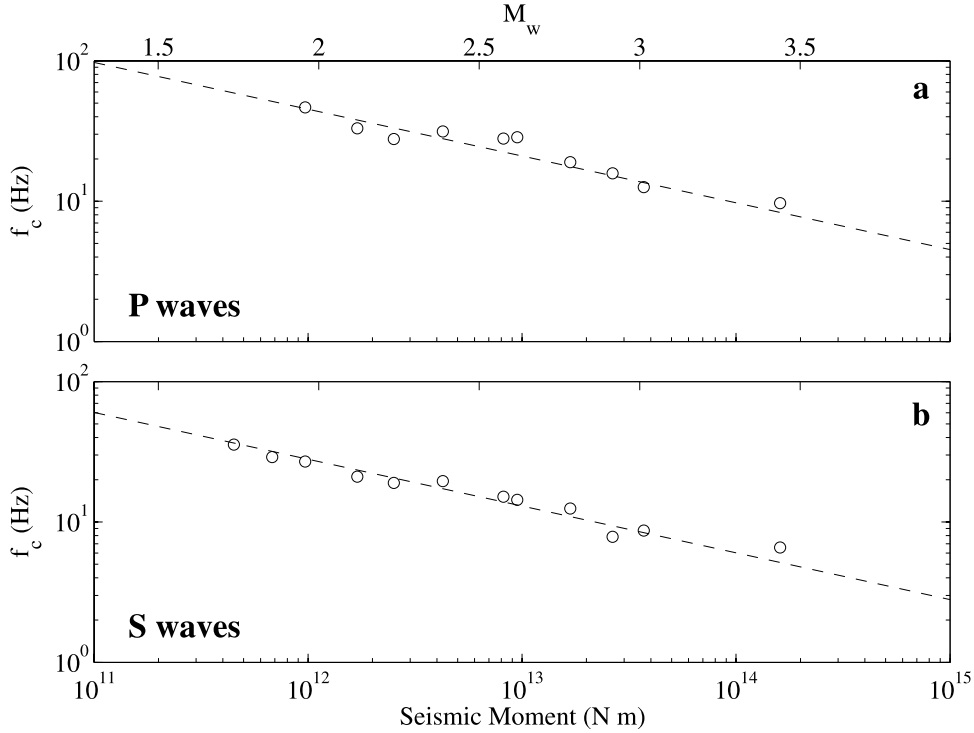

Figure 12. (a) *P* and (b) *S* corner frequencies versus moment, derived from the stacked spectra for the different moment bins. The results indicate $M_0 \propto f_c^{-3}$ as shown by the dashed lines. Error bars are shown for bins with more than three estimates.

Rivera, 2004] is to plot corner frequency versus seismic moment. As previously discussed, self-similarity predicts that $M_0 \propto f_c^{-3}$. We determined the relative seismic moment and corner frequencies for *P* and *S* waves independently (see Figure 12). The relative moment is scaled to obtain an approximation of the absolute seismic moment (see section 5). Corner frequencies follow the cube root scaling expected from self-similarity, as previously observed by *Ide et al.* [2003]. Of course, this is not surprising, given that the spectra themselves obey self-similarity scaling (see Figure 7 and prior discussion). Because of the corner frequency shift for *P* and *S* waves, we plot this relationship independently. It is possible that the 40 Hz and higher corner frequencies for the smaller moment bins are constrained less accurately than the corner frequencies for the larger earthquakes because our analysis extends only to 80 Hz. However, there are more earthquakes in the smaller moment bins, resulting in smoother stacked spectra (see Figures 7 and 8), which likely improves the reliability of the corner frequency estimates even when less of the spectrum is available. It is clear from Figures 7 and 12 that the available part of the spectra are consistent with the self-similarity hypothesis.

[36] The relationship between seismic moment and radiated seismic energy is also important and has been a focus of many previous studies. This relationship is commonly expressed in terms of apparent stress, defined as $\sigma_a = \mu E_s/M_0$. Figure 13 shows apparent stress plotted as a

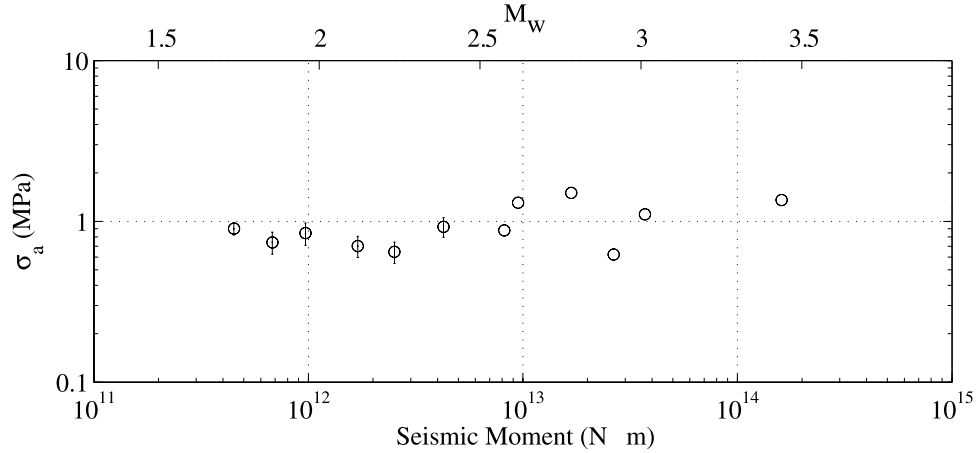

Figure 13. Apparent stress σ_a versus moment for the different moment bins. Apparent stress is nearly constant over M_W = 1.8 to 3.4, with an average value of about 1 MPa.

function of moment for our spectral stacks. The E_s/M_0 ratio is approximately constant as moment increases, as predicted if self-similarity is obeyed and apparent stress is constant as a function of earthquake size. Given the scatter in our data, a small degree of scaling is possible. A weighted least squares fit to the points in Figure 13 results in $E_s/M_0 \propto M_0^{0.08\pm0.10}$, providing relatively tight error bounds that include the zero exponent result expected from self-similarity.

[37] The average apparent stress is about 1 MPa, but for the reasons discussed above, this value is less well constrained than the relative σ_a between our different earthquake bins. The two largest sources of error in our absolute σ_a estimate are likely to be (1) our calibration factor between relative moment and M_W, and (2) the assumed S velocity at the source. Any calibration factor error will scale directly as M_0. From equation (8) we see that if, for example, our M_W estimates (assumed equal to the SCSN M_L values) are 0.2 units too large, this will result in σ_a estimates that are about 2 times too large. A 5% error in our assumed source S velocity will yield about 30% uncertainty in σ_a. Given these uncertainties and the scatter shown in Figure 13, a reasonable range for the possible values of the average apparent stress is 0.3–3.0 MPa.

7. Discussion

[38] Our study indicates that self-similarity of the earthquake source is consistent with data from over 400 small earthquakes in our study region, as shown by the scaling of source parameters such as corner frequencies and apparent stress as well as the similarity in the shapes of the source spectra themselves, independent of any particular source model. This conclusion is based on stacks of earthquake spectra in bins of similar seismic moment, a process that averages the properties of earthquakes in these bins. Spectra of individual earthquakes may also be obtained using our technique; these show much greater variability in corner frequency and apparent stress but their average properties are consistent with the results presented here. Although we do not take into account possible biasing effects, such as systematic changes in focal mechanism or rupture directivity, it is likely that these effects are minimized by averaging over stations at different distances and azimuths from the source region.

[39] Our study supports models in which the average apparent stress is constant as a function of earthquake size, as suggested by *Ide et al.* [2003] and others. Our results are limited by the small magnitude range spanned by our earthquakes ($1.8 \leq M \leq 3.4$ for the EGF-corrected data) but have sufficiently low scatter that fairly tight constraints can be placed on any possible moment dependence of apparent stress. *Mayeda and Walter* [1996] proposed that E_s/M_0 is proportional to $M_0^{1/4}$ over the magnitude range $3.3 \leq M \leq 7.3$, consistent with the suggestion of *Abercrombie* [1995] that apparent stress appears to increase gradually with moment over a magnitude range from 0 to 7. Such a strong dependence on M_0 is not supported by our results over the limited size range of our data (our best fitting scaling is $M_0^{0.08\pm0.10}$). Comparisons with other studies can extend the applicability of our results. Our estimated average apparent stress of 1 MPa is above most of the estimates of *Abercrombie* [1995] for similar size earthquakes (i.e., M_W = 1.8 to 3.4) and is consistent with the suggestion of *Ide and Beroza* [2001] that apparent stress has a nearly constant value of 1 MPa over the entire observed range of earthquake sizes.

[40] A large number of studies have suggested that the source spectra might have more complex behavior than that estimated from simple corner frequency models [e.g., *Singh and Ordaz*, 1994; *Mayeda and Walter*, 1996] and should include intermediate falloffs. Differences in the results obtained in different studies might be due to model assumptions that depend upon parametric data derived from the spectra rather than the spectra themselves. An advantage of our approach is that we can directly use the shapes of the spectra to test for self-similarity without any source model assumptions. A source of concern for our parametric analysis is whether the maximum frequency of 80 Hz that we use in our study is affecting our results, especially for estimates of the corner frequency for the smallest earthquakes. This does not appear to be a problem because we observe no saturation of the corner frequencies for the small events (see Figure 12).

[41] The values of apparent stress that we obtain have much less scatter than those seen in most previous studies, probably because of the averaging that we perform within each moment bin. Thus, although our study spans a quite limited magnitude range, our nearly constant values of apparent stress place fairly tight constraints on the amount of any scaling with moment that could be present within our data. Recently, *Mayeda et al.* [2004] have argued that a potential problem exists in comparing apparent stress for events over a broad region because the regional scatter of the estimates could make resolving scaling variations problematic. Also, some of the trends of previous studies might be masking (or exposing) the true trend, because of the large range of apparent stress uncertainties. Our study has the advantage of being restricted to a specific source region and of averaging over a large number of earthquakes, reducing the scatter and likely biases in our apparent stress estimates.

[42] Our results are limited to the cluster of earthquakes in our study region but the spectral stacking method should readily be applicable to other data sets. In particular, it would be useful to study clusters or aftershock sequences that contain larger earthquakes to extend the magnitude range. There are a number of possible candidates in southern California for such an analysis, including the Northridge and Landers aftershock sequences. In addition, studies of large numbers of distributed earthquakes, as recorded by local and regional seismic networks, might reveal spatial patterns in source properties. In this case, corrections for attenuation effects will be more complicated than when the earthquakes are restricted to a single cluster, but in principle, attenuation and source effects can be still be separated using a spectral stacking approach.

[43] **Acknowledgments.** We thank the personnel of IGPP and the Anza Seismic Group at UCSD who recorded, picked, and archived the seismograms. Rachel Abercrombie, Greg Beroza, Jack Boatwright, and Arthur McGarr provided useful comments and reviews. Funding for this research was provided by NEHRP/USGS grants 03HQPA0001 and 04HQAG0018. This research was also supported by the Southern California Earthquake Center. SCEC is funded by NSF Cooperative Agreement EAR-0106924 and USGS Cooperative Agreement 02HQAG0008. SCEC contribution 766.

References

Abercrombie, R. E. (1995), Earthquake source scaling relationships from −1 to 5 M_L using seismogram recorded at 2.5-km depth, *J. Geophys. Res.*, *100*, 24,015–24,036.

Abercrombie, R. E. (1996), The magnitude-frequency distribution of earthquakes recorded with deep seismometers at Cajon Pass, southern California, *Tectonophysics*, *261*, 1–7.

Aki, K. (1967), Scaling law of seismic spectrum, *J. Geophys. Res.*, *72*, 1217–1231.

Aki, K., and P. Richards (1980), *Quantitative Seismology*, 932pp., W. H. Freeman, New York.

Andrews, D. J. (1986), Objective determination of source parameters and similarity of earthquakes of different size, in *Earthquake Source Mechanics*, *Geophys. Monogr. Ser.*, vol. 37, edited by S. Das, J. Boatwright, and C. H. Scholz, pp. 259–267, AGU, Washington, D. C.

Berger, J., L. Baker, J. Brune, J. Fletcher, T. Hanks, and F. Vernon (1984), The Anza array: A high-dynamic-range, broadband, digitally radiometered seismic array, *Bull. Seismol. Soc. Am.*, *74*, 1469–1481.

Boatwright, J. A. (1980), A spectral theory for circular seismic sources: Simple estimates of source dimension, dynamic stress drop and radiated energy, *Bull. Seismol. Soc. Am.*, *70*, 1–27.

Boatwright, J. A., and J. B. Fletcher (1984), The partition of radiated energy between *P* and *S* waves, *Bull. Seismol. Soc. Am.*, *74*, 361–376.

Brodsky, E. E., and H. Kanamori (2001), Elastohydrodynamic lubrication of faults, *J. Geophys. Res.*, *106*, 16,357–16,374.

Brune, J. N. (1970), Tectonic stress and seismic shear waves from earthquakes, *J. Geophys. Res.*, *75*, 4997–5009.

Brune, J., S. Brown, and P. Johnson (1993), Rupture mechanics and interface separation in foam rubber models of earthquakes: A possible solution to the heat flow paradox and the paradox of large overthrusts, *Tectonophysics*, *218*, 59–67.

Choy, G. L., and J. L. Boatwright (1995), Global patterns of radiated seismic energy and apparent stress, *J. Geophys. Res.*, *100*, 18,205–18,228.

Frankel, A., J. Fletcher, F. Vernon, L. Haar, J. Berger, T. Hanks, and J. Brune (1986), Rupture characteristics and tomographic source imaging of $M_L \sim 3$ earthquakes near Anza, southern California, *J. Geophys. Res.*, *91*, 12,633–12,650.

Hanks, T. C., and D. M. Boore (1984), Moment-magnitude relations in theory and in practice, *J. Geophys. Res.*, *89*, 6229–6235.

Hough, S. E. (1997), Empirical Green's function analysis: Taking the next step, *J. Geophys. Res.*, *102*, 5369–5384.

Ide, S., and G. C. Beroza (2001), Does apparent stress vary with earthquake size?, *Geophys. Res. Lett.*, *28*, 3349–3352.

Ide, S., G. C. Beroza, S. G. Prejean, and W. L. Ellworth (2003), Apparent break in earthquake scaling due to path and site effects on deep borehole recordings, *J. Geophys. Res.*, *108*(B5), 2271, doi:10.1029/2001JB001617.

Izutani, Y., and H. Kanamori (2001), Scale-dependance of seismic energy-to-moment ratio for strike-slip earthquakes in Japan, *Geophys. Res. Lett.*, *28*, 4007–4010.

Jeffreys, H. (1942), On the mechanics of faulting, *Geol. Mag.*, *79*, 291.

Kanamori, H. (1977), The energy release in great earthquakes, *J. Geophys. Res.*, *82*, 2981–2987.

Kanamori, H., and T. H. Heaton (2000), Microscopic and macroscopic physics of earthquakes, in *Geocomplexity and the Physics of Earthquakes*, *Geophys. Monogr. Ser.*, vol. 120, edited by J. Rundle, D. L. Turcotte, and W. Kein, pp. 147–155, AGU, Washington, D. C.

Kanamori, H., and L. Rivera (2004), Static and dynamic scaling relations for earthquakes and their implications for rupture speed and stress drop, *Bull. Seismol. Soc. Am.*, *94*, 314–319.

Kanamori, H., J. Mori, E. Hauksson, T. H. Heaton, L. K. Hutton, and L. Jones (1993), Determination of earthquake energy release and M_L using TERRAscope, *Bull. Seismol. Soc. Am.*, *83*, 330–346.

Madariaga, R. (1976), Dynamics of an expanding circular fault, *Bull. Seismol. Soc. Am.*, *66*, 639–666.

Mayeda, K., and W. R. Walter (1996), Moment, energy, stress drop, and source spectra of western United States earthquakes from regional coda envelopes, *J. Geophys. Res.*, *101*, 11,195–11,208.

Mayeda, K., D. S. Dreger, W. R. Walter, G. Wurman, and F. Tajima (2004), BDSN Calibration for northern California earthquakes from coda-derived source spectra: Moment magnitude and radiated energy (abstract), *Seismol. Res. Lett.*, *75*, 278.

McGarr, A. (1999), On relating apparent stress to the stress causing earthquake fault slip, *J. Geophys. Res.*, *104*, 3001–3003.

Melosh, J. (1979), Acoustic fluidization: A new geologic process?, *J. Geophys. Res.*, *84*, 7512–7520.

Mori, J., R. E. Abercrombie, and H. Kanamori (2003), Stress drops and radiated energies of aftershocks of the 1994 Northridge, California, earthquake, *J. Geophys. Res.*, *108*(B11), 2545, doi:10.1029/2001JB000474.

Mueller, C. S. (1985), Source pulse enhancement by deconvolution of an empirical Green's function, *Geophys. Res. Lett.*, *12*, 33–36.

Park, J., C. R. Lindberg, and F. L. Vernon (1987), Multitaper spectral analysis of high frequency seismograms, *J. Geophys. Res.*, *92*, 12,675–12,648.

Scott, J. S., T. G. Masters, and F. L. Vernon (1994), 3-D velocity structure of the San Jacinto fault zone near Anza, California-I. *P* waves, *Geophys. J. Int.*, *119*, 611–626.

Sibson, R. (1973), Interactions between temperature and pore-fluid pressure during earthquake faulting and a mechanism for partial or total stress relief, *Nature*, *243*, 66–68.

Singh, S. K., and M. Ordaz (1994), Seismic energy release in Mexican subduction zone earthquakes, *Bull. Seismol. Soc. Am.*, *84*, 1533–1550.

Vernon, F. L. (1989), Analysis of data recorded on the Anza Seismic Network, Ph.D. thesis, Scripps Inst. of Oceanogr., Univ. of Calif., San Diego, La Jolla.

Warren, L. M., and P. M. Shearer (2000), Investigating the frequency dependance of mantle *Q* by stacking *P* and *PP* spectra, *J. Geophys. Res.*, *105*, 25,391–25,402.

Warren, L. M., and P. M. Shearer (2002), Mapping lateral variations in upper mantle attenuation by stacking *P* and *PP* spectra, *J. Geophys. Res.*, *107*(B12), 2342, doi:10.1029/2001JB001195.

D. Kilb, G. A. Prieto, P. M. Shearer, and F. L. Vernon, Institute of Geophysics and Planetary Physics, University of California, San Diego, 9500 Gilman Drive, La Jolla, CA 92093, USA. (dkilb@epicenter.ucsd.edu; gprieto@epicenter.ucsd.edu; pshearer@ucsd.edu; flvernon@ucsd.edu)